Structure and magnetic properties of magnetron-sputtered Fe/Cu multilayered thin films

S. F. Cheng, A. N. Mansour,* J. P. Teter, K. B. Hathaway, and L. T. Kabacoff
Naval Surface Warfare Center, Dahlgren Division, White Oak Detachment, Research and Technology Department, 10901 New Hampshire Avenue, Silver Spring, Maryland 20903-5000
(Received 2 March 1992; revised manuscript received 14 July 1992)

The structure and magnetic properties of Fe/Cu multilayered films with a constant total Fe thickness of 1050 Å but varying Fe-layer thickness from 6.3 to 42 Å and varying Cu to Fe thickness ratio from 1 to 3 were investigated using x-ray diffraction (XRD), x-ray absorption fine-structure (XAFS) spectroscopy, and magnetic measurements. Samples were prepared at room temperature on mica, glass, and silicon substrates using the dc-magnetron-sputtering method. For films with the same Fe-layer thickness, it was found that the magnetic moment of Fe decreases with increasing thickness ratio of Cu to Fe. For films with a Cu to Fe thickness ratio of 3, it was found that the magnetic moment of Fe decreases with decreasing thickness of the individual Fe layers. XRD and XAFS results revealed that in the multilayered films, Cu has a well-defined fcc structure with minimal amount of structural disorder independent of the individual layer thickness or thickness ratio. On the other hand, quantitative analysis of EXAFS data revealed that the crystal structure of Fe changes with decreasing thickness of the Fe layers from distorted bcc (for 42- and 21-Å-thick Fe layers) to fcc (for 10.5- and 6.3-Å-thick Fe layers) in films with the Cu layer three times thicker than the Fe layer. The single-phase fcc Fe of the 6.3-Å Fe/19-Å Cu multilayered film was found to have a lattice constant of 3.596 Å and is ferromagnetic with a Curie temperature of 210 K and a spontaneous magnetization of ~ 690 emu/cm^3.

INTRODUCTION

The magnetic properties of face-centered-cubic (fcc) γ-Fe stabilized by thin-film growth have attracted much attention in recent years.[1,2] Particular interest has been focused on the Fe/Cu system, since at room temperature the lattice mismatch between γ-Fe with lattice constant $a=3.59$ Å extrapolated from high-temperature data[3] and Cu with lattice constant $a=3.6148$ Å is very small, and hence is favorable for epitaxial growth. In addition, bulk Fe and Cu are mutually insoluble, which limits the amount of interdiffusion at the interface. According to total-energy-band calculations,[4] γ-Fe can exist in a nonmagnetic, ferromagnetic, or antiferromagnetic state at a lattice constant near that of Cu. This has led to many conflicting accounts of the magnetic properties of γ-Fe grown on Cu.[3] It was found that the magnetic state which γ-Fe assumes is strongly dependent on experimental parameters. Recent work by Magnan *et al.*[5] using surface extended x-ray-absorption fine-structure spectroscopy revealed a correlation between the magnetic properties and the crystallographic structure of the γ-Fe films. They observed that films that are antiferromagnetic have a well-defined fcc structure, while films generally found to be ferromagnetic have a distorted fcc structure. There is also no general agreement on the maximum thickness of γ-Fe attainable by epitaxial growth of Fe on Cu. Among molecular-beam-epitaxy grown films, the maximum thickness ranges from 5 to 17 monolayers.[6,7]

Fe/Cu multilayered films are less well studied. Komuro *et al.*[8] grew Fe/Cu multilayered films on Si substrates at 150 °C using the rf magnetron sputtering method. They found that the crystal structure of the films depends on the thickness of individual Fe and Cu layers. Single-phase fcc Fe was obtained for Fe film thickness of 17 Å and Cu film thickness of 49 or 98 Å. In both cases, the Fe films were found to be discontinuous.[9] Their results also showed that the saturation magnetization of fcc Fe is 1.32 T. This is in disagreement with the work by Schuller,[10] who found that single-phase fcc Fe of Fe/Cu multilayer films grown at room temperature with similar film thicknesses as those of Komuro *et al.*[8] have a very low magnetic moment. This suggests that the influence of process parameters is still not well understood, and the relationship between the structures and magnetic properties remains to be clarified.

In this study, Fe/Cu multilayered films were grown using the dc magnetron sputtering method. The films were grown at room temperature to minimize interdiffusion of Cu and Fe. The crystal structures were characterized by x-ray-diffraction and x-ray-absorption fine-structure (XAFS) spectroscopy which is an element-specific probe of the local atomic structure. The objectives of this study are (i) to investigate the crystal structures of Fe and Cu as a function of film thickness and (ii) to determine if face-centered-cubic Fe can be stabilized by sputtering in a Cu/Fe multilayer structure. An attempt is made to correlate the crystal structures with the magnetic properties of the grown Fe/Cu multilayered films.

EXPERIMENT

Sample preparation

The Fe and Cu single-layered films and the Fe/Cu multilayered films were prepared at room temperature on mica, glass, and Si substrates using the dc magnetron sputtering method. Research-grade high-purity Fe and

Cu targets (99.9 and 99.99%, respectively) were employed in preparing the samples. Deposition of the films was made by sputtering from the targets operating at a power of 30 W. Substrates were mounted on a simultaneously rotating and revolving fixture to ensure uniformity of film thickness. The system was evacuated to 5×10^{-7} torr and back filled with argon to 3.5 mTorr prior to sputtering. Deposition rates were 4.2 and 9.5 Å/min for Fe and Cu, respectively. These rates were determined using a profilometer from films deposited under the same conditions. A series of films with Fe layer thickness ranging from 6.3 to 42 Å and Cu layer thickness of 1, 2, or 3 times the Fe layer thickness was fabricated. A Cu buffer layer of about 200 Å was first deposited. This step was followed by the Fe/Cu multilayer deposition and then the deposition of a 200-Å Cu overlayer. The total Fe thickness in each of the multilayered film samples is 1050 Å. The thickness of individual layers was varied by manually controlling the duration of the target shutters in the open and closed positions. A single-layer Fe film of 1050-Å thickness covered by 200 Å of Cu and a single-layer Cu film of 3300 Å were also deposited for calibration purposes. The layer thicknesses for the various samples are listed in Table I.

X-ray diffraction and XAFS measurements

The crystal structures of the grown films were investigated using monochromatized Cu $K\alpha$ x rays. All samples were examined by high-angle (2θ from 30° to 100°) x-ray diffraction (XRD). In addition, to check for superlattice lines, low-angle θ-2θ XRD measurements were performed from 1° to 7° for samples grown on glass substrates.

The x-ray absorption experiments were performed on beamline X-11A (Ref. 11) at National Synchrotron Light Source (NSLS) with the storage ring operating at an electron energy of 2.5 GeV and a stored current in the range of 110–220 mA. Data were collected with a variable-exit double-crystal monochromator using two flat Si(111) crystals. Harmonics were rejected by detuning the parallelism of the monochromator crystals. This is achieved by a piezoelectric transducer to adjust the top crystal until the harmonic content is minimized. Spectra of the Fe K edge (7112.0 eV) and Cu K edge (8980.0 eV) for the thin-film samples were obtained with the fluorescence-detection mode[12] using a specialized fluorescence ion chamber detector.[13] The x-ray intensities were monitored using ionization chambers filled with nitrogen gas for the incident beam, an appropriate mixture of nitrogen and argon gases for the transmitted beam, and krypton gas for fluorescence signal. The background component due to elastic and Compton scattering of the incident x rays was minimized using an aluminum Soller slit assembly and Mn and Ni filters, each with an effective thickness of three absorption lengths, for the Fe K edge and Cu K edge, respectively. Only the Fe/Cu multilayered films with thickness ratio of 1 to 3 grown on glass substrates were investigated using XAFS spectroscopy. Reference samples of bulk Fe (5-μm-thick foil), bulk Cu (7.5-μm-thick foil), and a 3300-Å-thick Cu film deposited on glass substrate were also investigated to serve as standards for comparison purposes and subsequent data analysis. The XAFS measurements for both foils were made in the transmission mode and that of the 3300-Å Cu film in the fluorescence mode. All spectra presented here were measured at room temperature (300 K).

Magnetic measurements

The magnetic measurements were performed at room temperature using a vibrating sample magnetometer. A maximum field of 5 kOe was applied either parallel or perpendicular to the film plane. The field and temperature dependencies of the magnetic moments of selected samples were also measured with a superconducting quantum interference device (SQUID) magnetometer.

RESULTS AND DISCUSSION

XRD results

All samples were examined by x-ray diffraction. For those grown on mica and silicon, the Fe and Cu peaks are overwhelmed by the diffraction peaks from the substrates and, thus, little structural information were extracted. The following discussion is limited to samples grown on

TABLE I. Layer thickness, crystal structure, and spontaneous magnetization of the grown films.

Sample	No. of bilayers	d_{Fe} (Å)[a]	d_{Cu} (Å)[b]	Structure[c]	Magnetization (emu/cm^3)[d]
A	1	1050.0		bcc	1530
B	25	42.0	40.0	bcc	1545
C	25	42.0	80.0	bcc	1487
D	25	42.0	124.0	Distorted bcc	1391
E	50	21.0	62.0	Distorted bcc	1144
F	100	10.5	31.0	fcc	150
G	167	6.3	19.0	fcc	0
H	1		3300.0	fcc	

[a]Thickness of individual Fe layer.
[b]Thickness of individual Cu layer.
[c]Crystal structure of the Fe films as determined by XRD and/or EXAFS except for sample *H*, where it represents that of the Cu film. Due to lack of XAFS data on samples *B* and *C*, the assignment of their structures was based only on the XRD results.
[d]Room-temperature spontaneous magnetization of the Fe films.

glass substrates. No obvious texturing was observed for any of the samples. The x-ray-diffraction patterns of samples *B*, *C*, and *D*, which have a constant Fe thickness (42 Å) and a varied Cu to Fe thickness ratio of 1, 2, and 3 are shown in Fig. 1(a). The patterns of the single-layered Fe (bcc) and Cu (fcc) films are included for comparison. The small Cu peaks present in the single-layered Fe film are due to the deposited Cu overlayer. For all three samples, the (110) bcc Fe peak, which has the highest intensity can be easily identified as a shoulder on the high-angle side of the (111) fcc Cu peak. This indicates that the majority of Fe in these samples possesses a bcc crystal structure.

Figure 1(b) shows the x-ray-diffraction patterns of samples *D*–*G* and the single-layered Fe and Cu films. It can be seen that the line broadening due to the overlapping of the (110) bcc Fe and (111) fcc Cu peaks is reduced with decreasing thickness of the Fe layer. For samples *D* and *E*, the (110) Fe peak is identifiable indicating that the majority of Fe in these two samples is bcc. However, the (110) Fe peak for samples *F* and *G* cannot be seen, suggesting that most of the Fe in both samples has a fcc structure. It was observed that after annealing sample *F* at 300 °C for 2 h, the XRD pattern shows sharp peaks characteristics of bcc Fe. Cu in all of the samples possesses a fcc structure as expected.

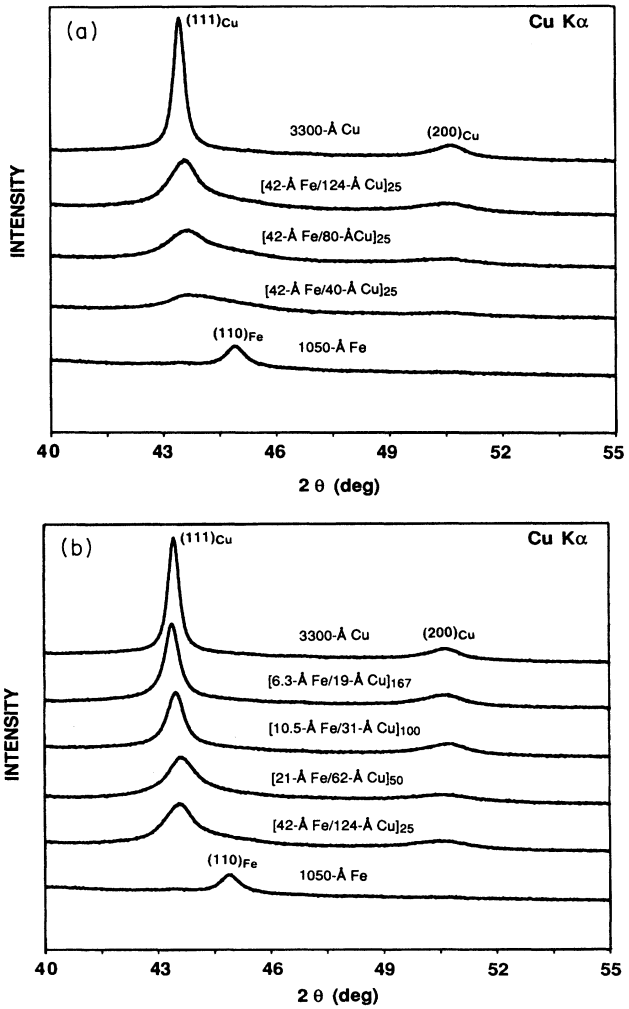

FIG. 1. (a) X-ray-diffraction patterns of samples *B*, *C*, and *D*, which have a constant Fe thickness (42 Å) and a varied Cu-to-Fe thickness ratio, and of single-layered Fe and Cu films. (b) X-ray-diffraction patterns of samples *D*–*G*, which have a constant Cu-to-Fe thickness ratio of 3:1 and of single-layered Fe and Cu films.

Figure 2 shows the low-angle x-ray-diffraction patterns of samples *E* through *G*. As can be seen, superlattice lines were present for all of the three samples (and also others, not shown here), which indicate the periodic nature of these films. The modulation wavelength of sample *F* calculated from the positions of the first- and second-order superlattice lines is 44.6 Å, which agrees rather well with the expected value of 41.5 Å. The calculated wavelengths of sample *G* using the first-order line and that of sample *E* using the second-order line have less than 5% deviation from their proposed values. We would like to note that a new set of samples with similar film thicknesses, recently prepared under the same conditions except with the use of computer-controlled target shutters, showed much stronger superlattice lines. Thus, we believe that the weak intensity of the superlattice lines observed for the current samples is due to a slight irregularity in the periodicity caused by manually controlling the targets' shutters during deposition of the films rather than intermixing of Fe and Cu atoms.

XAFS results

The crystal structure of these films was further examined by XAFS spectroscopy. Although the structure of interest is that of Fe, the local structure of both Cu and Fe were investigated. The experimentally measured x-ray-absorption cross section $\mu_0(E)x$, where E is the x-ray photon energy and x is the sample thickness, is given by

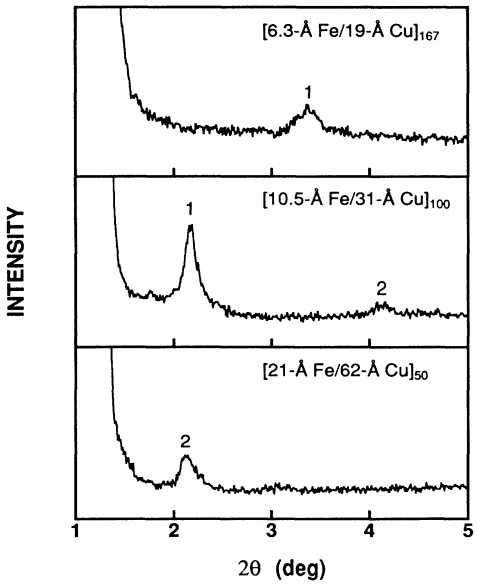

FIG. 2. Low-angle x-ray-diffraction patterns of samples *G*, *F*, and *E* showing superlattice lines.

$\ln(I_0/I)$ for transmission data and I_f/I_0 for fluorescence data with I_0, I, and I_f being the incident, transmitted, and fluorescence yield intensities, respectively. In determining $\mu_0 x$, correction for the energy dependence of the incident x-ray intensity in the fluorescence measurements is made using cross sections calculated with McMaster coefficients.[14] The pre-edge background absorption $\mu_p(E_n)x$ is determined from a quadratic fit to the data roughly 300–30 eV below the edge energy and then extrapolated over the entire range of the spectrum. The K-edge absorption $\mu(E)x$ is then isolated by subtracting $\mu_p(E)x$ from $\mu_0(E)x$. The smoothly varying atomic absorption $\mu_a(E)x$ was determined by fitting the post-edge data of $\mu(E)x$ with a cubic spline function.[15,16] An energy-independent step normalization is applied by dividing $\mu(E)x$ by the value of the atomic absorption $\mu_a(E_n)x$, where E_n is the normalization energy and is taken to be 100 eV above the edge energy.

The normalized x-ray-absorption near-edge structure (XANES) of the Cu K edge for the multilayered films of samples D, F, and G and the 3300-Å-thick Cu film (sample H) are shown in Fig. 3. These spectra are compared with the XANES spectra of structurally well-known polycrystalline Cu foil with fcc lattice. The spectra display the normalized K-edge absorption μ as a function of photoelectron energy. The zero energy is assigned to the peak of the first feature at the onset of the edge. The data for all the edges are plotted on the same scale with the upper spectra shifted vertically for clarity of presentation. All spectra are indistinguishable from each other, indicating that Cu in the Fe/Cu multilayered films and the 3300-Å Cu film retains the chemistry and structure of the fcc lattice of bulk Cu foil. That is, the chemistry of Cu in the Fe/Cu multilayered films is independent of the number of Fe/Cu layers and their thicknesses.

The normalized XANES spectra of the Fe K edge for the multilayered films of samples $D-G$ are shown in Fig. 4. These spectra are compared with the XANES spectra of polycrystalline Fe foil with bcc lattice and polycrystalline Cu foil with fcc lattice. For the K edge of the Cu foil, the zero-energy assignment is as described in the preceding paragraph. For the Fe K edge of the Fe foil and the multilayered films, the peak position of the feature at the onset of the edge is not as well defined as in the case of Cu foil. Therefore, the zero energy is assigned to the first minima in the first derivative of $\mu(E)$ with respect to photoelectron energy. The data for all the edges are again plotted on the same scale with the upper spectra shifted vertically for clarity of presentation.

Visual comparison of the data from Fe and Cu foils, as examples of bcc and fcc structures, provides an indication of the sensitivity of the XANES to variations in the local coordination geometry of the absorbing atom. The local coordination geometry up to four coordination spheres of Fe metal with bcc lattice consists of 8, 6, 12, and 24 Fe atoms at 2.483, 2.867, 4.054, and 4.754 Å, respectively.[17,18] That of Cu metal with fcc lattice consists of 12, 6, 24, and 12 Cu atoms at 2.556, 3.615, 4.427, and 5.112 Å, respectively.[18,19] Accordingly, from comparisons of the Fe and Cu K-edge data of the multilayered films with K-edge data of Fe and Cu foils, one should be able to infer the Fe and Cu local coordination geometry in the multilayered films. That is, what type of lattice (bcc versus fcc) does iron occupy in the multilayered films?

Examination of the Fe K-edge XANES data of the multilayered films reveals that the XANES of samples D and E are very similar and resemble very closely that of metallic Fe foil with a bcc lattice. Thus, it is concluded that the local coordination geometry of the majority of Fe in the multilayered films of samples D and E is con-

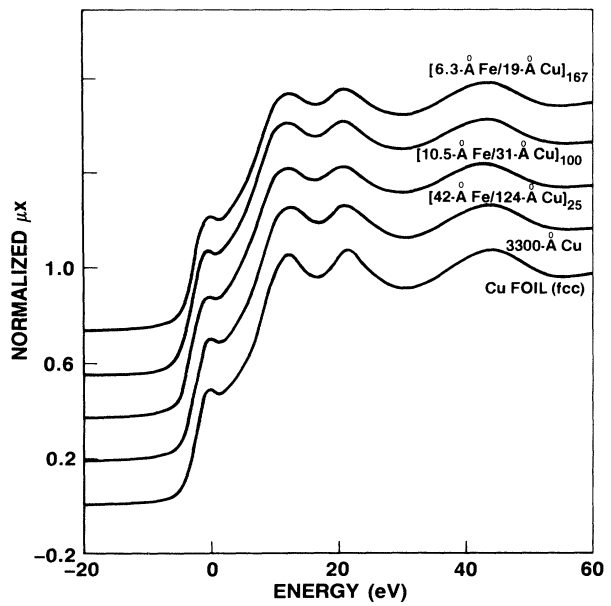

FIG. 3. Comparison of normalized Cu K-edge XANES data for fcc Cu foil, a 3300-Å Cu film (sample H), and Fe/Cu multilayered of samples D, F, and G.

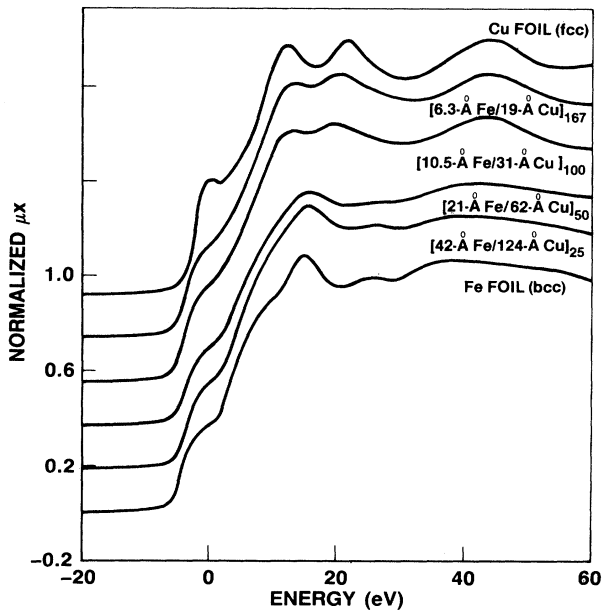

FIG. 4. Comparison of normalized Fe K-edge XANES data for bcc Fe foil, Fe/Cu multilayered films of samples D, E, F, and G, and fcc Cu foil.

sistent with that of a bcc lattice. Furthermore, the XANES data of samples F and G are also very similar. However, their XANES resemble very closely that of metallic Cu with a fcc lattice rather than that of Fe foil with a bcc lattice. Hence, it is concluded that the local coordination geometry of the majority of Fe in the multilayered films of samples F and G is consistent with that of a fcc lattice.

Next, we turn attention to the extended x-ray-absorption fine-structure (EXAFS) region of the XAFS spectrum from which structural information such as coordination numbers, distances, and disorder (which includes both the dynamic thermal disorder term and the static structural disorder term) are easily obtained via least-squares fits of filtered k-space amplitudes. The normalized EXAFS data, $\chi(k)$, are given by

$$\chi(k)=\left[\frac{\mu(k)-\mu_a(k)}{\mu_a(k_n)}\right]\left[\frac{\mu_m(k_n)}{\mu_m(k)}\right], \quad (1)$$

where k is the photoelectron wave number and $\mu(k)$ and $\mu_a(k)$ are as described previously. The term, $\mu_m(k)$, is the atomic absorption calculated with McMaster coefficients,[14] which provides the energy-dependent McMaster normalization and k_n is the photoelectron wave number corresponding to the normalization energy E_n. The energy-dependent normalization is necessary if one chooses to use theoretical backscattering amplitude and phase values such as those calculated with the FEFF program[20] to extract the structural parameters.

The normalized Cu K-edge EXAFS data, $\chi(k)$, of the Fe/Cu multilayered films (samples D, F, and G) and the 3300-Å Cu film (not shown) are very similar to the $\chi(k)$ of fcc Cu foil [shown in Fig. 6(b)]. The frequencies of the EXAFS oscillations match very closely those of Cu foil. A slight reduction in the amplitude of the EXAFS oscillation for the multilayered films and the 3300-Å Cu film from that of bulk Cu foil is observed. Fourier transforms of Cu K-edge EXAFS data for the Fe/Cu multilayered films and the 3300-Å Cu film (not shown) are also similar to that of fcc Cu foil except for a small reduction in the amplitude of the peaks. The reduction in the amplitude of the peaks is mainly due to self-absorption of the fluorescence signal by the sample and structural disorder in the film samples as will be shown from quantitative analysis of the data later in the text. Therefore, it is concluded that the local geometry of Cu in the Fe/Cu multilayered films is consistent with that of a fcc lattice in agreement with previous conclusions based on comparisons of Cu K-edge XANES data.

The normalized Fe K-edge $\chi(k)$ data for the Fe/Cu multilayered films are displayed in Fig. 5. The $\chi(k)$ data from sample D are compared with data from sample E [Fig. 5(a)] and the $\chi(k)$ data from sample F are compared with data from sample G [Fig. 5(b)]. As can be seen from Fig. 5, the $\chi(k)$ data from sample D is almost identical to that from sample E, yet these spectra are clearly quite different [Fig. 5(c)] from the almost indistinguishable spectra of samples F and G. Furthermore, the Fe K-edge $\chi(k)$ data from samples D and G are compared in Figs. 6(a) and 6(b) with Fe K-edge $\chi(k)$ data of bcc Fe foil and Cu K-edge $\chi(k)$ data of fcc Cu foil, respectively. Also, comparisons of Fourier transform data of the Fe K-edge $k^3\chi(k)$ data from samples D and G with Fourier transforms of bcc Fe foil and fcc Cu foil are shown in Figs. 7 and 8, respectively. The peak positions in the Fourier-transform data of sample D are similar to those in the Fourier transform of bcc Fe rather than those in the Fourier transform of fcc Cu foil. For sample G, the peak positions in the Fourier transform data, on the other hand, are similar to those in the Fourier transform of fcc Cu rather than those in the Fourier transform of bcc Fe foil. Variations in the amplitude of Fourier transform data of the Fe/Cu multilayered films from those of Fe and Cu foils data are due to self-absorption of fluorescence signal by the samples and structural disorder as will be shown later in the text. Based on these results, it is concluded that the local coordination geometry of samples D and E is similar to that of bcc Fe and the local coordination geometry of samples F and G is similar to that of fcc Cu. These conclusions are also in agreement with those obtained from comparisons of the Fe XANES data.

Quantitative analysis methods for the structure information contained in the first peak of the Fourier transform (i.e., $\Delta r = 1.30-3.04$ Å for both Fe and Cu data)

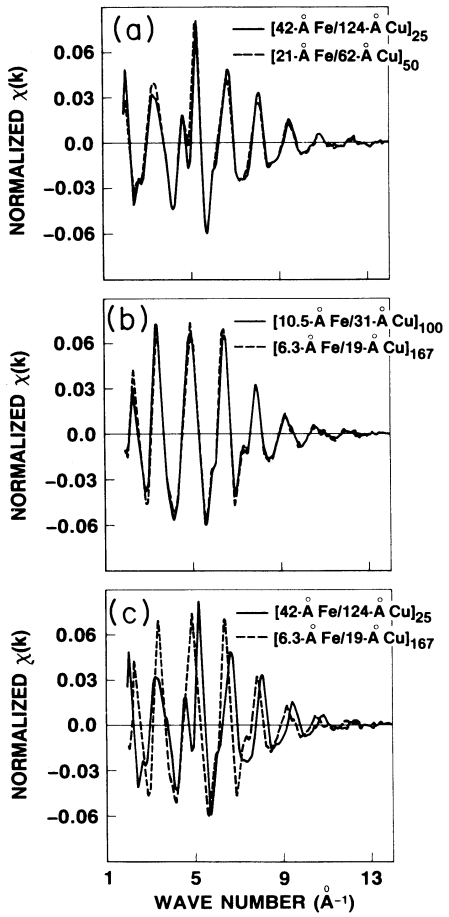

FIG. 5. Comparison of normalized Fe K-edge EXAFS data, $\chi(k)$, for samples D and E (a), samples E and G (b), and samples D and G (c).

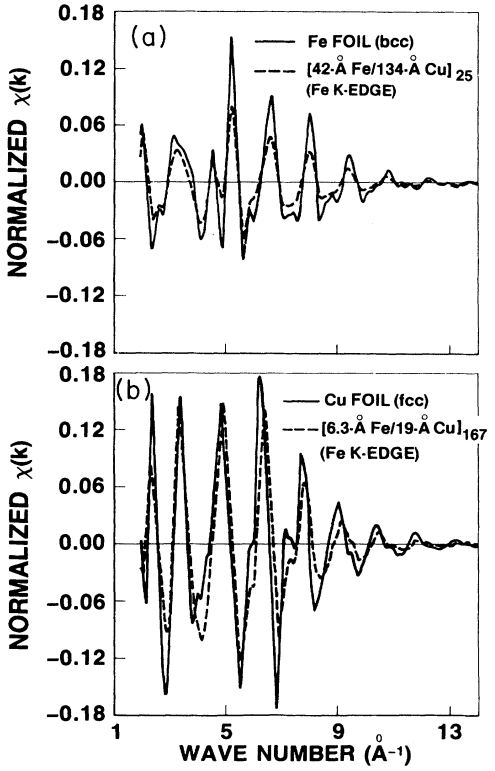

FIG. 6. Comparison of normalized Fe K-edge EXAFS data, $\chi(k)$, for sample D and bcc Fe foil (a) and normalized Fe K-edge EXAFS data, $\chi(k)$, for sample G and normalized Cu K-edge EXAFS data, $\chi(k)$, for fcc Cu foil (b).

will now be presented. This part of the Fourier transform is filtered and back transformed into k space to allow quantitative analysis of k-space amplitudes and phases using standard procedures. For polycrystalline materials and in the dipole approximation, the filtered EXAFS data is related to the structural parameters by

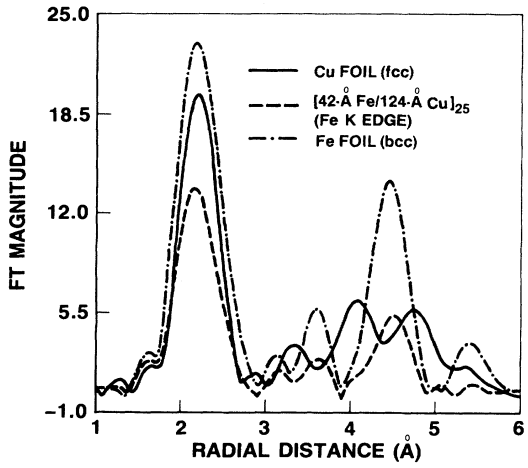

FIG. 7. Comparison of the Fourier transform of normalized Cu K-edge EXAFS data, $k^3\chi(k)$, for fcc Cu foil (Δk: 1.98–12.92 Å^{-1}), Fe K-edge of sample D (Δk: 2.24–12.88 Å^{-1}) and bcc Fe foil (Δk: 2.18–12.90 Å^{-1}).

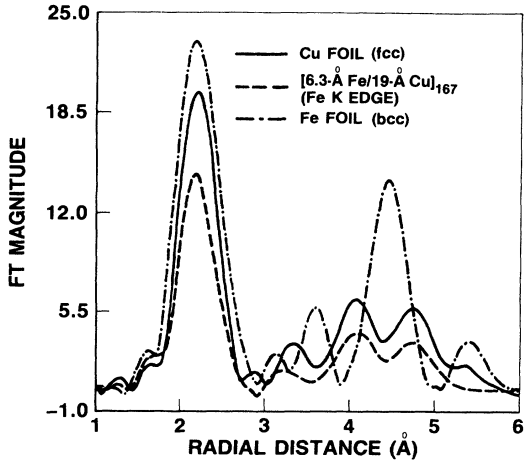

FIG. 8. Comparison of the Fourier transform of normalized Cu K-edge EXAFS data, $k^3\chi(k)$, for fcc Cu foil (Δk: 1.98–12.92 Å^{-1}), Fe K-edge of sample G (Δk: 2.12–13.09 Å^{-1}) and bcc Fe foil (Δk: 2.18–12.90 Å^{-1}).

$$\chi(k) = -\sum_i C_i(k)\sin[2kR_i + 2\delta(k) + \phi_i(k)] , \qquad (2)$$

where the index i denotes a specific type of atom located at an average distance R_i from the central absorbing atom. The terms $\delta(k)$ and $\phi(k)$ represent the modification in the phase shift of the ejected photoelectron wave function by the potential of the central absorbing and backscattering atoms, respectively. The amplitude term $C_i(k)$ is given by

$$C_i(k) = \frac{N_i}{KR_i^2} S_0^2 A(k) F_i(\pi,k,R) e^{-2(R_i/\lambda)} e^{-2\sigma_i^2 k^2} , \qquad (3)$$

where N_i is the number of atoms of the ith type at distance R_i. The term σ_i is the disorder or root-mean-square deviation about the average distance R_i and includes both a dynamic term arising from the thermal motion of the atoms and a static term describing structural disorder. The other terms λ, $F_i(\pi,k,R)$, and $A(k)$ represent the electron mean free path, the magnitude of the effective curved-wave backscattering amplitude for the ith type of atoms and central atom losses, respectively. Finally, S_0^2 is an energy-independent many-body amplitude reduction factor.[20]

In fitting the EXAFS data with Eq. (3), four parameters per shell are usually varied: coordination number (N), coordination distance (R), disorder squared (σ^2), and an inner potential energy shift (E_0), which is used in the definition of the photoelectron wave number k. Since, the information content of the EXAFS data is bandwidth limited, the maximum number of fit parameters must not exceed the number of independent data points $N_{\rm pts}$ given by the formula, $N_{\rm pts} = 2\Delta k \Delta R/\pi$, where Δk is the k-space range over which $\chi(k)$ is fitted and ΔR is the filtered R-space range of the Fourier transform.[21,22] All fits were done in the k range of 3.0–12.5 Å^{-1} with k^3 weighted filtered data. For all fits a Δk of 9.5 Å^{-1} and a ΔR of 1.74 Å were used and, hence, the

maximum number of parameters that can be varied is equal to 10.

For the analysis of Cu K-edge EXAFS data a single-shell fit is sufficient, and, thus, a maximum of four floating parameters [which is less than the maximum number of allowable variables that can be used in Eq. (2)] are needed in the fit. The Cu data were fitted using both empirical and theoretical standards. Results of numerical fits using empirical phase and backscattering amplitude values determined from Cu foil data are listed in Table II. Next, $A(k)$, $\lambda(k)$, $\delta(k)$, $\phi(k)$, and $F(\pi,k,R)$ values determined with the FEFF program[20] for a cluster of $CuCu_{12}$ with $R_{Cu\text{-}Cu}=2.556$ Å were used to fit the Cu data. In fitting the Cu foil data we have constrained the coordination number N to the value of 12 and varied S_0^2, R, σ^2, and E_0. The many-body amplitude reduction factor (S_0^2) is determined to be 0.856 and this value will be used in analyzing Cu-Cu interactions in all other samples. The distance (R) is determined to be 2.535 Å, which is less by $\delta R=0.021$ Å from the crystallographic distance of 2.556 Å and this value of δR will be used to correct all Cu-Cu distances analyzed with theoretical standards. The disorder (σ^2) is determined to be 8.1×10^{-3} Å^2, which is slightly higher than the theoretically determined value of 7.7×10^{-3} Å^2 giving a $\delta\sigma^2=-0.40\times10^{-3}$ Å^2 that will be used to correct all Cu-Cu fit disorders analyzed with theoretical standards.[23] For all other samples, the Cu K-edge filtered data was fitted with S_0^2 set equal to 0.856 and varied N, R, σ^2, and E_0. Results of these numerical fits are also listed in Table II.

The Fe data were analyzed using only theoretical standards due to lack of an appropriate empirical standard. The Fe foil data cannot be used as reference to analyze Fe-Fe interactions due to the proximity of the first and second coordination spheres in bcc Fe. The Fe foil and samples D and E with bcc Fe were analyzed using a two-shell fit with Fe-Fe model data for both shells. Filtered EXAFS data of samples F and G with fcc Fe were analyzed using either a single-shell fit with Fe-Fe model data or a two-shell fit with Fe-Fe and Fe-Cu model data. In these two samples, the fraction of Fe atoms at the Fe/Cu interface is large enough to require a second shell of Fe-Cu interactions. Therefore, values for $A(k)$, $\lambda(k)$, $\delta(k)$, $\phi(k)$, and $F(\pi,k,R)$ were determined with the FEFF program[20] for a cluster of $FeFe_8$ with $R_{Fe\text{-}Fe}=2.485$ Å. In addition, samples F and G with fcc Fe were analyzed using theoretical standards calculated for a cluster of $FeFe_{12}$ with $R_{Fe\text{-}Fe}=2.540$ Å. These results were essentially the same as those based on the first cluster, and, hence, only the former results will be reported. Model data for the Fe-Cu interactions were determined from a cluster of $FeCu_{12}$ with $R_{Fe\text{-}Cu}=2.540$ Å. In fitting the Fe foil data, N_1 and N_2 were fixed to their crystallographic values of 8 and 6, respectively. In addition, one inner potential parameter E_0 was used for both shells. Thus, the parameters that were free to vary were S_0^2, R_1, R_2, σ_1^2, σ_2^2, and E_0. From this fit, a many-body amplitude reduction factor (S_0^2) of 0.781 and corrections of δR_1 of 0.013 Å, $\delta R_2=0.021$ Å, $\delta\sigma_1^2=0.45\times10^{-3}$ Å^2, and $\delta\sigma_2^2=0.76\times10^{-3}$ Å^2 were obtained. The Fe data in the multilayered films with bcc lattice were fitted using S_0 equal to 0.781 and varied N_1, R_1, R_2, σ_1^2, σ_2^2, and E_0 and N_2 being constrained to equal $0.75N_1$. The Fe data of the multilayered films with a fcc lattice were fitted first with a single shell with S_0^2 set equal to 0.781 and varied N_1, R_1, σ_1^2, and E_0. Second, a two-shell fit with Fe-Fe and Fe-Cu interactions, was made using S_0 equal to 0.781 and varied N_1, N_2, R_1, σ_1^2, σ_2^2, and E_0 with R_2 being constrained to equal R_1. The two-shell fit yielded a significantly better fit relative to the single-shell fit by virtue of roughly a 50% reduction in the sum of the square of residuals. Results of these numerical fits for Fe in the Fe/Cu multilayered films are listed in Table III.

TABLE II. Summary of structural results using least-square fits of Cu K-edge EXAFS for the 3300-Å Cu film and the Fe/Cu multilayered films. Uncertainties in the coordination number (N), coordination distance (R), mean-square relative displacement in R (σ^2), and inner potential corrections (E_0) were estimated at ±10%, ±0.01 Å, ±10%, and ±0.5 eV, respectively.

Sample	N	R (Å)	σ^2 (10^{-3} Å^2)	E_0 (eV)
Bulk fcc Cu[a]	12.00	2.556	7.70	−1.8
H[b]	11.61	2.558	8.10	−2.0
H[c]	11.56	2.558	8.37	−0.1
D[b]	11.30	2.554	8.96	−1.3
D[c]	11.23	2.553	8.90	0.7
F[b]	11.55	2.557	8.74	−1.2
F[c]	11.50	2.556	8.70	0.8
G[b]	10.92	2.555	7.62	−1.4
G[c]	10.87	2.556	7.58	0.4

[a]Known structural parameters for fcc Cu foil are listed for comparison purposes (Refs. 18 and 19).

[b]Fits were performed using central atom losses, electron mean free path, phase, and backscattering amplitude values determined theoretically with the FEFF program for a cluster of $CuCu_{12}$ with $R_{Cu\text{-}Cu}=2.556$ Å.

[c]Fits were performed using empirically determined phase and backscattering amplitude values from Cu foil EXAFS data.

The coordination numbers in Table II and III include corrections due to self-absorption of fluorescence signal. The magnitude of reduction due to this effect on the coordination numbers and disorders were determined using equations derived by Tan, Budnick, and Heald.[24] These reductions in the coordination numbers were estimated to be 5 and 7 % for Cu data of the 3300-Å Cu film and the Fe/Cu multilayered films, respectively, and 9 % for the Fe data. Self-absorption corrections to the disorder parameter were determined to be very small, of the order of 0.08×10^{-3} Å^2, and were neglected.

The following conclusions can be made from inspection of the data in Tables II and III. For Cu data (Table II), the structural parameters obtained on the basis of empirical standards are essentially the same as those obtained with the use of theoretical standards. The structural parameters for all samples are consistent with those of a fcc lattice as expected. The coordination numbers and distances for all samples are nearly the same within the quoted uncertainty and resemble those of bulk Cu ($N=12$ and $R=2.556$ Å). The disorder in all samples within the quoted uncertainty is nearly the same as that of bulk Cu disorder of 7.7×10^{-3} Å^2 indicating that the

Cu structural disorder in the multilayered films is negligible.

For the Fe data (Table III), the structural parameters are consistent with those of a bcc lattice (samples *D* and *E*) or a fcc lattice (samples *F* and *G*). Within the quoted uncertainty, the coordination numbers are similar to those of a bcc lattice (samples *D* and *E*) or a fcc lattice (samples *F* and *G*). The coordination distance of the first and second shells for samples *D* and *E* are very similar to those expected for a bcc lattice, i.e., 2.483 and 2.867 Å, respectively, except for a slight reduction in the second shell distance (R_2) of sample *E*. The disorders for samples *D* and *E* of both the first and second coordination spheres are significantly higher than those of bulk bcc Fe (compare with $\sigma_1^2=5.09\times10^{-3}$ Å^2 and $\sigma_2^2=6.6\times10^{-3}$ Å^2) indicating a high degree of structural disorder. The degree of structural disorder in the second coordination sphere of sample *E* is also significantly increased relative to that of sample *D*. For both samples, the increase in the disorder of the second coordination sphere is significantly larger than that of the first coordination sphere suggesting a specific type of lattice distortion which only significantly affects the second coordination sphere. These results are consistent with a tetragonally distorted bcc lattice in which the *c* axis expands, while both the *a* and the *b* axes contract equally in such a way to keep the unit-cell volume the same as that of the unperturbed bcc lattice. With this type of lattice distortion, the second shell of bcc Fe splits into two subshells with four Fe atoms at a smaller distance and two Fe atoms at a larger distance than that of the unperturbed bcc second-shell distance. The degree of splitting in the second shell of bcc Fe depends on the degree of lattice distortion. These two subshells, when analyzed in terms of a single shell, result in a high level of structural disorder. Our results indicate that the degree of lattice distortion in sample *E* is greater than that of sample *D* (i.e., increases with decreasing film thickness). This observation combined with the fact that both samples *F* and *G* consist of fcc Fe suggest a critical film thickness below which the fcc lattice is more stable than the distorted bcc lattice. Quantification of the degree of lattice distortion, which requires detailed analysis of the structure of higher coordination spheres is currently underway and will be published later. For samples *F* and *G*, the first-shell coordination distances (results from the two-shell fit) indicate a fcc Fe lattice with lattice constant of 3.581 and 3.596 Å, respectively. Although the disorder of the first shell of the Fe-Fe interaction in samples *F* and *G* is larger than that of the first shell of bulk bcc Fe, it is very similar to that of the first shell of bulk fcc Cu. The larger disorder for the Fe-Cu interaction relative to that of the Fe-Fe interaction in both samples is due to structural disorder introduced by the presence of the interface and to a smaller degree due to Cu and or Fe interdiffusion. Although both samples *F* and *G* show a fcc structure, a small amount of bcc Fe phase in both samples cannot be ruled out.

Quantitative analysis of recently acquired EXAFS data for sample *A* (1050 Å single layer Fe film) reveals a perfect bcc structure similar to that of bulk Fe foil, as expected.

TABLE III. Summary of structural results using least-squares fits of Fe *K*-edge EXAFS data for the Fe/Cu multilayered films. Uncertainties in the coordination number (N), coordination distance (R), mean-square relative displacement in R (σ^2), and inner potential corrections (E_0) were estimated at ±10%, ±0.01 Å, ±10%, and ±0.5 eV, respectively. Underlined quantities assert that these parameters were constrained during the fit. Fits were performed using central atom losses, electron mean-free-path, phase, and backscattering amplitude values determined theoretically with the FEFF program for a cluster of $FeFe_8$ with $R_{Fe\text{-}Fe}=2.485$ Å.

Sample	N	R (Å)	σ^2 (10^{-3} Å^2)	E_0
Bulk bcc Fe[a]	8.00	2.483	5.09	−3.0
	6.00	2.867	6.60	−3.0
D[b]	7.27	2.491	6.93	−2.1
	5.45	2.855	12.51	−2.1
E[b]	7.38	2.497	6.62	−2.5
	5.53	2.832	18.24	−2.5
F[c]	9.21	2.537	7.84	−2.3
F[d] Fe-Fe	5.91	2.532	7.14	−1.5
Fe-Cu	5.24	2.532	12.64	−1.5
N-total	11.15			
G[c]	10.68	2.552	8.21	−3.2
G[d] Fe-Fe	5.39	2.543	8.43	−1.9
Fe-Cu	6.41	2.543	10.94	−1.9
N-total	11.80			

[a]Known structural parameters for bcc Fe foil are listed for comparison purposes (Refs. 17 and 18).
[b]Data analyzed using a two-shell fit with Fe-Fe model data for both.
[c]Data analyzed using a single-shell fit.
[d]Data analyzed using a two-shell fit with Fe-Fe and Fe-Cu model data.

Magnetic properties

Figure 9 shows the room-temperature spontaneous magnetization of samples *A*–*G* grown on mica substrates

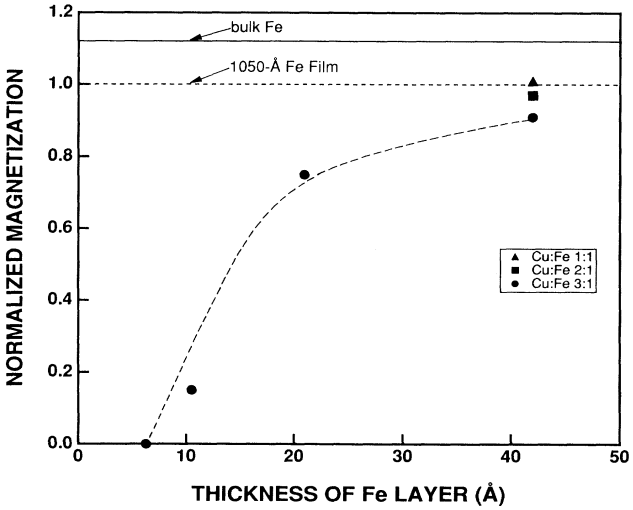

FIG. 9. Room-temperature magnetization of samples *A*–*G*, grown on mica substrates, normalized to the Fe single-layered film (sample *A*).

normalized to the Fe single-layer film. Similar results were obtained for the films grown on the other two types of substrates (i.e., glass and silicon). The magnetization of the 1050-Å Fe film was found to be 1530 emu/cm^3, compared to the 1714 emu/cm^3 of bulk Fe. This is probably due to the reduced density in the thin-film form.[8] For films having a constant Fe layer thickness, the magnetic moments were found to decrease with increasing Cu-to-Fe thickness ratio (samples $B-D$). Since the number of layers is the same, the decrease in moment may be caused by the presence of a small amount of fcc Fe, which could be paramagnetic at room temperature (see below). The decrease in the magnetic moment from sample D to E can be explained by either the increase of Fe and Cu interaction at the interfaces due to the increased number of bilayers or the increased proportion of fcc Fe, or both. Another possibility of the reduced moment is due to the distorted bcc structure as suggested by the

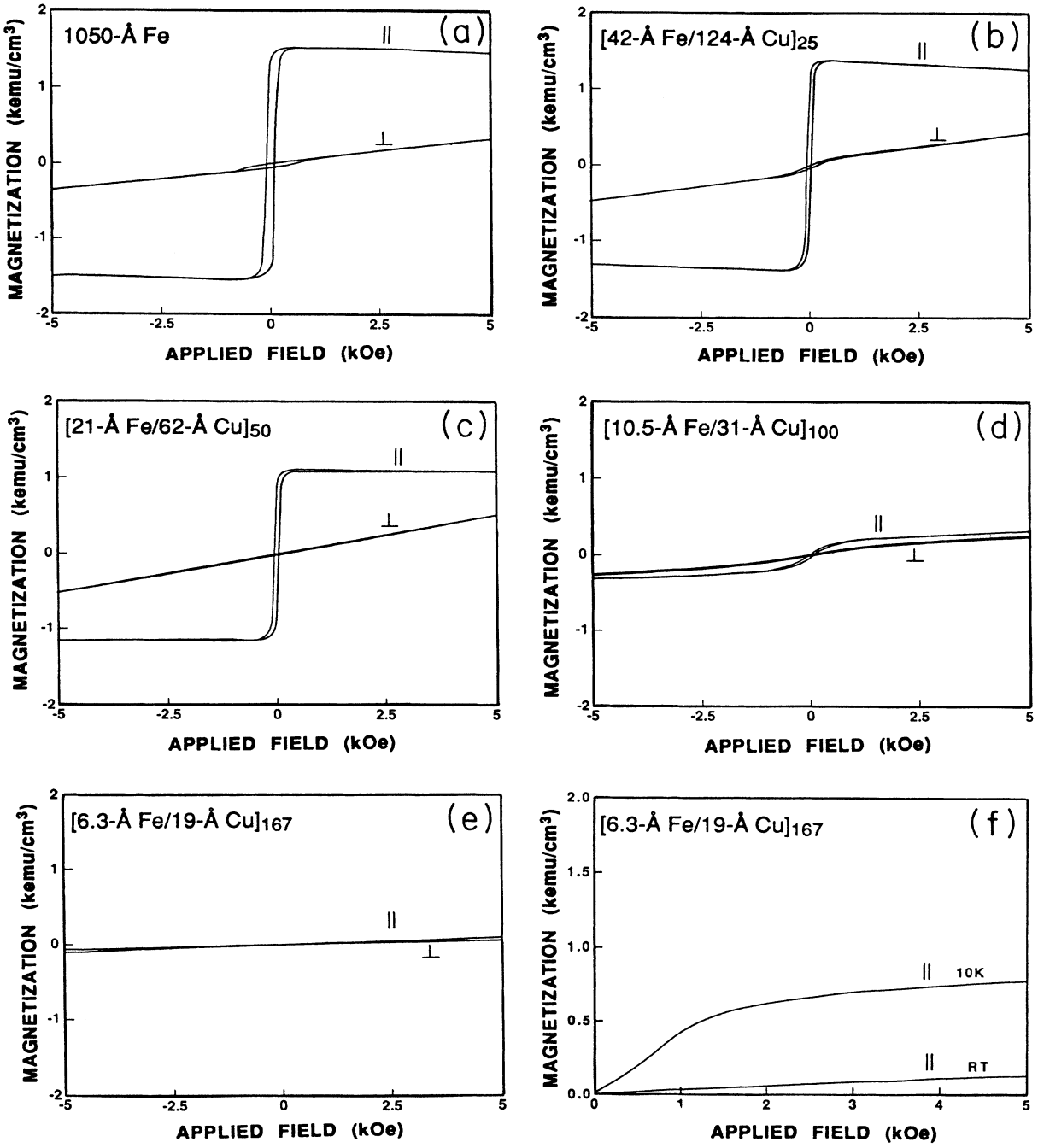

FIG. 10. (a)–(e) Room-temperature hysteresis loops of samples A and $D-G$ grown on mica and (f) first-quadrant magnetization curves at 300 and 10 K for sample G grown on glass. $\parallel$ and $\perp$ are for samples measured with the film plane parallel and perpendicular to the field direction, respectively.

EXAFS result. The sudden drop of the magnetic moment from sample E to F cannot be explained by the Fe-to-Cu interaction alone. The decrease is mainly due to the fact that the majority of Fe in sample F occurred in the fcc structure as deduced from the structural analysis. Sample G with the minimum thickness of Fe (6.3 Å or 3.5 monolayers) shows no spontaneous magnetization at room temperature. Since the structure of Fe in the Fe/Cu film of sample G is shown to assume that of a fcc lattice, this suggests that at this thickness and at room temperature, γ-Fe is paramagnetic. The magnetization values for all samples are listed in Table I. Figures 10(a)–10(e) show the hysteresis loops of samples A and D–G (grown on mica), for field directions both parallel and perpendicular to the film plane. It appears that the anisotropy favoring the in-plane orientation is reduced with decreasing Fe thickness.

Figure 10(f) shows the magnetization curves in the direction parallel to the film plane of sample G grown on glass, measured at 300 and 10 K using a SQUID magnetometer. Similar to the sample grown on mica [Fig. 10(e)], no spontaneous magnetization was observed at 300 K. However, at 10 K, the sample shows a magnetization of $\sim$690 emu/cm^3 (8.6 kG). The thermomagnetic curve of the same sample measured under a field of 5 kOe is shown in Fig. 11. By using the conventional M^2-versus-T plot, the magnetic transition was estimated to be 210 K. The broadness of this transition could be due to the distribution of the layer thicknesses occurring due to manually controlling the target shutters during the growth process or to the largeness of the applied field. From our quantitative XAFS analysis, the lattice constant of the single-phase fcc Fe (sample G) is 3.596 Å. According to total-energy-band calculations, at this lattice constant, γ-Fe can be in a nonmagnetic or antiferromagnetic state with the latter as the lower-energy state.[4] In contrast to theory, our experimental results seem to suggest that γ-Fe is ferromagnetic at low temperature and paramagnetic at 300 K with the transition around 210 K. The structure of this γ-Fe is a well-defined fcc structure similar to that of three Fe monolayers of a Cu-Fe-Cu sandwich structure.[5] This conclusion is based on the fact that our Fourier transforms of EXAFS data for samples F and G display well defined second, third, and fourth coordination spheres. Furthermore, our disorder values are similar to those of the ordered rather than the distorted fcc structure. Thus, this results does not agree with that of Magnan *et al.*, who suggested that ferromagnetic fcc Fe has a distorted lattice, while a well-ordered fcc Fe lattice is characteristic of anitferromagnetic or paramagnetic samples.[5]

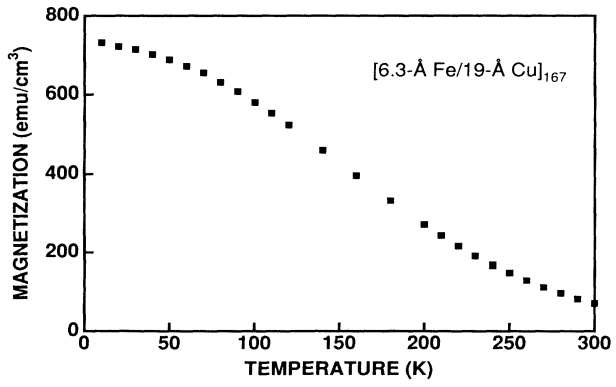

FIG. 11. Thermomagnetic curve of sample G measured at a field of 5 kOe.

The critical thickness of fcc Fe stabilized in our experiment is also a point of interest. Assuming the room-temperature magnetic moment of sample F derives from the presence of bcc Fe, it is then estimated that the amount of bcc Fe is roughly 10%. Such a small amount cannot be ruled out on the basis of EXAFS data. Therefore, the maximum thickness of purely fcc Fe stabilized in magnetron-sputtered Fe/Cu multilayers is about five monolayers. Above this thickness, samples are likely to contain both fcc and bcc or only bcc Fe.

SUMMARY

The structure and magnetic properties of Fe/Cu multilayered films were investigated using x-ray diffraction, x-ray-absorption fine-structure spectroscopy, and magnetic measurements. It was found that the room-temperature magnetization decreases with increasing Cu-to-Fe thickness ratio or decreasing thickness of individual Fe layer. XRD and XAFS results indicate that in the multilayered films, Cu has a well-defined fcc structure with a minimal amount of structural disorder, while the crystal structure of Fe changes with decreasing Fe thickness from tetragonally distorted bcc (42- and 21-Å-thick Fe layers) to fcc (10.5- and 6.3-Å-thick Fe layers) in films with a Cu-to-Fe layer thickness ratio of 3. The single-phase fcc Fe of the 6.3-Å-Fe/19-Å-Cu multilayered film was found to have a lattice constant of 3.596 Å and is ferromagnetic with a Curie temperature of 210 K and a spontaneous magnetization around 690 emu/cm^3 of Fe.

ACKNOWLEDGMENTS

We acknowledge the support of the U.S. Department of Energy, Division of Materials Sciences, under Contract No. DE-AS05-80-ER10742 for its role in the development and operation of Beam Line X-11 at the National Synchrotron Light Source (NSLS). The NSLS is supported by the Department of Energy, Division of Materials Sciences and Division of Chemical Sciences, under Contract No. DE-AC02-76CH00016. This work is supported in part by the Independent Research Program and the Technology Base Office of the Naval Surface Warfare Center (Dahlgren Division, White Oak Detachment). The authors would like to thank Dr. Jim Krebs of NRL for his discussion and help on the SQUID measurements and Dr. C. L. Chien at Johns Hopkins University for conducting the low-angle x-ray-diffraction experiment.

*To whom all inquiries should be sent at the following address: Naval Surface Warfare Center, Dahlgren Division, White Oak Detachment, Code R34, Bldg. 30-213, 10901 New Hampshire Avenue, Silver Spring, MD 20903-5000.

[1]L. M. Falicov, D. T. Pierce, S. D. Bader, R. Gronsky, K. B. Hathaway, H. J. Hopster, D. N. Lambeth, S. S. P. Parkin, G. A. Prinz, M. Salamon, I. K. Schuller, and R. H. Victoria, J. Mater. Res. **5**, 89 (1990).

[2]G. A. Prinz, J. Magn. Magn. Mater. **100**, 469 (1991).

[3]S. H. Lu, J. Quinn, D. Tian, F. Jona, and P. M. Marcus, Surf. Sci. **209**, 364 (1989).

[4]V. L. Moruzzi, P. M. Marcus, and J. Kubler, Phys. Rev. B **39**, 6957 (1989).

[5]H. Magnan, D. Chandesris, B. Villette, O. Heckmann, and J. Lecante, Phys. Rev. Lett. **67**, 859 (1991).

[6]D. Pescia, M. Stampanoni, G. L. Bona, A. Vaterlaus, R. F. Willis, and F. Meier, Phys. Rev. Lett. **58**, 2126 (1987).

[7]Y. Darici, J. Marcano, H. Min, and P. A. Montano, Surf. Sci. **182**, 477 (1987).

[8]M. Komuro, Y. Kozono, S. Narishige, M. Hanazono, and Y. Sugita, IEEE Trans. Magn. **MAG-23**, 3701 (1987).

[9]Y. Kozono, M. Komuro, S. Narishige, M. Hanazono, and Y. Sugita, J. Appl. Phys. **61**, 4311 (1987).

[10]I. K. Schuller (private communication).

[11]D. E. Sayers, S. M. Heald, M. A. Pick, J. I. Budnick, E. A. Stern, and J. Wong, Nucl. Instrum. Methods **208**, 631 (1983).

[12]J. Jaklevic, J. A. Kirby, M. P. Klein, A. S. Robertson, G. S. Brown, and P. Eisenberger, Solid State Commun. **23**, 679 (1977).

[13]F. W. Lytle, R. B. Greegor, D. R. Sandstrom, E. C. Marques, J. Wong, C. L. Spiro, G. P. Huffman, and F. E. Huggins, Nucl. Instrum. Methods **226**, 542 (1984).

[14]W. H. McMaster, N. Kerr Del Grande, J. H. Mallet, and J. H. Hubbell, *Compilation of X-ray Cross Sections* (National Technical Information Service, Springfield, VA, 1969).

[15]D. E. Sayers and B. A. Bunker, in *X-Ray Absorption, Principles, Applications, Techniques of EXAFS, SEXAFS and XANES,* edited by D. C. Koningsberger and R. Prins (Wiley, New York, 1988), pp. 211–253.

[16]J. W. Cook, Jr. and D. E. Sayers, J. Appl. Phys. **52**, 5024 (1981).

[17]*Pearson's Handbook of Crystallographic Data for Intermetallic Phases,* edited by P. Villars and L. D. Calvert (American Society of Metals, Metals Park, Ohio, 1985), Vol. 3, p. 2162.

[18]B. Rupp, B. Smith, and J. Wong, J. Appl. Crystallography **24**, 263 (1991).

[19]*Pearson's Handbook of Crystallographic Data for Intermetallic Phases* (Ref. 17), Vol. 2, p. 1922.

[20]J. J. Rehr, J. Mustre de Leon, S. I. Zabinsky, and R. C. Albers, J. Am. Chem. Soc. **113**, 5136 (1991).

[21]F. W. Lytle, D. E. Sayers, and E. A. Stern, Physica B **158**, 701 (1989).

[22]Report on the International Workshops on Standards and Criteria in XAFS, in *X-Ray Absorption Fine Structure,* edited by S. S. Hasnain (Horwood, Chichester, UK, 1991), Chap. 195, p. 751.

[23]E. Sevillano, H. Meuth, and J. J. Rehr, Phys. Rev. B **20**, 4908 (1979).

[24]Z. Tan, J. Budnick, and S. M. Heald, Rev. Sci. Instrum. **60**, 1021 (1989).